



ALMA MATER STUDIORUM  
UNIVERSITÀ DI BOLOGNA

ARCHIVIO ISTITUZIONALE  
DELLA RICERCA

Alma Mater Studiorum Università di Bologna  
Archivio istituzionale della ricerca

Pt-WO<sub>3</sub> oxydehydrates fructose to furans in the gas phase

This is the final peer-reviewed author's accepted manuscript (postprint) of the following publication:

*Published Version:*

*Availability:*

This version is available at: <https://hdl.handle.net/11585/898252> since: 2023-04-23

*Published:*

DOI: <http://doi.org/10.1016/j.cej.2021.132337>

*Terms of use:*

Some rights reserved. The terms and conditions for the reuse of this version of the manuscript are specified in the publishing policy. For all terms of use and more information see the publisher's website.

This item was downloaded from IRIS Università di Bologna (<https://cris.unibo.it/>).  
When citing, please refer to the published version.

(Article begins on next page)

This is the final peer-reviewed accepted manuscript of:

Davide Carnevali, Adrien D'Oliveira, Marco G. Rigamonti, Fabrizio Cavani, Gregory S. Patience "Pt-WO<sub>3</sub> oxydehydrates fructose to furans in the gas phase", Chemical Engineering Journal 429 (2022) 132337

The final published version is available online at:  
<https://doi.org/10.1016/j.cej.2021.132337>

Terms of use:

Some rights reserved. The terms and conditions for the reuse of this version of the manuscript are specified in the publishing policy. For all terms of use and more information see the publisher's website.

*This item was downloaded from IRIS Università di Bologna (<https://cris.unibo.it/>)*

***When citing, please refer to the published version.***

# Pt-WO<sub>3</sub> oxidehydrates fructose in the gas phase

Davide Carnevali<sup>a</sup>, Adrien D'Oliveira<sup>a</sup>, Marco G. Rigamonti<sup>a</sup>, Fabrizio Cavani<sup>b</sup>, Gregory S. Patience<sup>a,\*</sup>

<sup>a</sup>*Chemical Engineering Department, 2900 Edouard Montpetit Blvd, Montreal, H3T 1J4, Canada*

<sup>b</sup>*Dipartimento di Chimica Industriale, Viale del Risorgimento, 4, 40136 Bologna, Italy*

---

## Abstract

Bio feedstocks are destined to replace fossil fuels for specialty chemicals but current biorefineries mainly ferment hexose—the most abundant feedstock—to ethanol. The maximum theoretical carbon atom efficiency of this process is 67% but the market price of biofuels is several-fold lower than biochemicals and monomers. We report for the first time a gas phase catalytic process that dehydrates fructose to 5-hydroxymethyl furfural (HMF). A two-fluid nozzle atomized aqueous solutions of fructose into a fluidized bed operating at 350 °C. The solution forms an aerosol (droplet size of 30 μm), which contacts the hot Pt-WO<sub>3</sub>/TiO<sub>2</sub> catalyst and reacts to HMF rather than caramelizing. The maximum yield reached 21% and it increased slightly with temperature, and decreased with increasing catalyst inventory; it was less sensitive to O<sub>2</sub> concentration, Pt loading on the catalyst, liquid feed flowrate, and fructose feed concentration. At the optimal condition, selectivity continued to increase with time even after 3 h reaction. HMF as starting material presents a selectivity to DFF of 42%, with a conversion of 86% at 250 °C.

*Keywords:* fluidized, gas, sugar, platinum, atomization, 5-hydroxymethyl furfural, furfural,

---

## 1. Introduction

The elevated oxygen/carbon ratio of carbohydrates versus petroleum constitutes an advantage to produce specialty chemicals and monomers. Sugar fermentation to bio-ethanol dominates the market at a maximum theoretical carbon atom yield of 67% [1]. However, specialty chemicals command prices several-fold higher than that of bioethanol at fuel value. Fructose dehydrates to 5-hydroxymethyl furfural (HMF), a green intermediate, with a greater selectivity than glucose due to the similar spatial conformation and the faster enolisation reaction (Figure 1) [2]. Hydrogen reacts with HMF to dimethyl

---

\*Corresponding author

*Email address:* gregory-s.patience@polymtl.ca (Gregory S. Patience)

10 furan and dimethyl tetrahydrofuran (Figure 1)—a biofuel [3, 4]— while the hydrogenolytic ring opening produces adipic acid—a monomer for nylon-6,6 [5]. Oxygen reacts with HMF to 2,5-diformyl furan [6, 7, 8] and further to 2,5-furandicarboxylic acid (FDCA) [9, 10] (Figure 1). FDCA is the furanic substitute of terephthalic acid, which is a promising substitute for polyethylene  
15 terephthalate. Avantium developed the YXY technology that converts HMF to an ether with methanol/ethanol followed by an oxidation step to FDCA [11, 12]. Acidic catalysts, ionic liquids, and supercritical water dehydrate fructose and glucose to HMF [13, 14, 15, 16, 17, 18, 19]. Organic solvents are necessary to extract the product otherwise HMF hydrolyzes to levulinic acid and formic acid,  
20 or polymerizes to insoluble compounds—humins [20, 21, 22] (Figure 1).

Sn-Beta zeolite in tetrahydrofuran and water convert carbohydrates at 70 % selectivity [23]. Other organic solvents include alkylphenol [24], dimethylsulfoxide (DMSO) and methylisobutylketone [25, 26] and ethyl acetate [27]. These processes require contact times that range from minutes to hours because of the  
25 poor mass and heat transfer characteristics of multiphase (liquid) reactors.

Metal-based catalysts [9, 10, 28, 29, 30, 31] or enzymatic processes [32, 33, 34] oxidize HMF to FDCA. Tandem processes in a single vessel reduces complexity like the multiphase reactor with methyl-isobutyl ketone and 2-butanol as organic phase (**author?**) [35]; the aqueous solution dehydrates fructose to HMF,  
30 while the organic phase extracts it and further oxidize to FDCA [36]. Pt/C oxidehydrates fructose to FDCA in  $\gamma$ -valero lactone and H<sub>2</sub>O [37]. Combination of ionic liquids and not-noble metals avoid the organic phase and allows the one pot reaction [38]. Fluidized bed reactors operate at higher temperature with superior mass transfer and, consequently, reaction rates orders of magnitude  
35 higher. FBRs pyrolyze biomass into energy and chemicals [39]. Glass beads in an FBR cracks aqueous solutions of sugar sparged into the bed [40, 41] Fast pyrolysis of cellulose in FBRs approach 62 % yields of levoglucosan, 3.5 % of HMF and 1 % of furfural [42]. Immobilized anaerobic sludge produces biohydrogen and bioethanol [43]. A magnetically stirred fluidized bed reactor ferments glu-  
40 cose to ethanol within 95 % of the theoretical yield [44]. Two anaerobic fluidized bed reactors at 55 °C product H<sub>2</sub> and ethanol molar fractions of 58.9 % fro a xylose-glucose mixture [45].

We demonstrated the versatility of atomizing liquids into catalytic fluidized beds: VPO partially oxidizes xylose to C2-C4 carboxylic acids [46]; WO<sub>3</sub>/TiO<sub>2</sub>  
45 dehydrates glycerol to acrolein [47, 48] and decarbonylates fructose to furfural [49]; and, Keggin-type catalyst oxidehydrates 2-methyl,1-3-propanediol to methacrylic acid [50]. Here we investigated fructose dehydration to HMF in a  $\mu$ -fluidized bed reactor. A nozzle atomized the aqueous liquid feed directly into the catalytic bed. We screened temperature, O<sub>2</sub> concentration, catalyst load-  
50 ing, Pt content on the catalyst, liquid flowrate, feed fructose mass concentration with a Plackett-Burman experimental design. The experimental plan was based on three levels of temperature and O<sub>2</sub>:fructose molar ratio and two levels for catalyst loading.

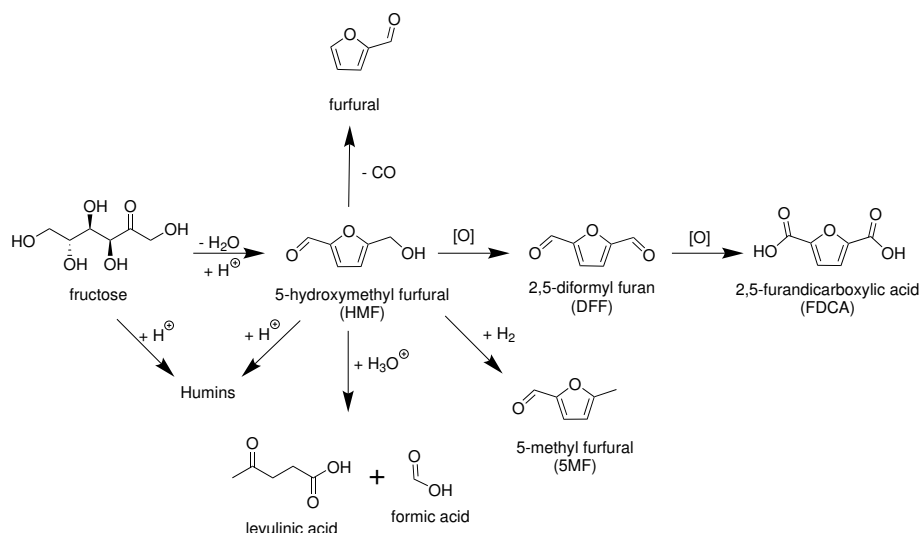


Figure 1: Fructose dehydrates to HMF. Organic solvents suppress the polymerization to humins and the rehydration to levulinic acid and formic acid. Decarbonylation leads to furfural, while the hydrogenation produces 5MF. HMF oxidation gives DFF and further FDCA, the furanic substitute of terephthalic acid.

## 2. Experimental section

55 A furnace heated a 15 mm ID by 400 mm high quartz tube. Three thermocouples measured the temperature along the length at 20 mm below the bed, 5 mm — inside the bed, 90 mm above the distributor, and a fourth monitored the temperature in the exit line. The reactor operated at 1.4 bar while the  $\Delta P$  between the inlet and outlet—0.001 bar during the reaction. A quartz frit,

60 with a porosity of 150  $\mu\text{m}$  to 200  $\mu\text{m}$ , ensured the gas was distributed uniformly across the reactor diameter (Figure 2). A stream of O<sub>2</sub> in Ar fluidized the catalytic bed and burned the coke formed during the reaction. A nozzle atomized the aqueous fructose solution into the Pt-WO<sub>3</sub>/TiO<sub>2</sub> catalytic bed. An HPLC pump metered the liquid solution feedrate while 50 mL min<sup>-1</sup> of argon atomized it to produce an effervescent spray (Figure 3c) with droplets less than 30  $\mu\text{m}$

65 to minimize catalyst agglomeration and blocking the nozzle. A ceramic tube enveloped the injector to reduce the heat transfer and ensure that the solvent evaporated in the bed rather than the injector; when the temperature exceeded 100 °C, solvent evaporated in the line and the sugar crystallized and blocked it.

70 A stream of 50 mL min<sup>-1</sup> of argon flushed the annular space between the injector and ceramic tube. The exit line (uninsulated) fed into a quench in an ice bath. The quench fluid contained 25 g dimethyl sulfoxide to improve furanic solubility and 25 g H<sub>2</sub>O. An on-line mass spectrometer (MS) with a multiple ion detector monitored non-condensable gas concentrations—CO, CO<sub>2</sub>, O<sub>2</sub>, Ar, CH<sub>4</sub>, while

75 an HPLC quantified the liquid samples collected each 15 min during the first hour and then each 30 min until the end of the experiment (Figure 2). Glycerol

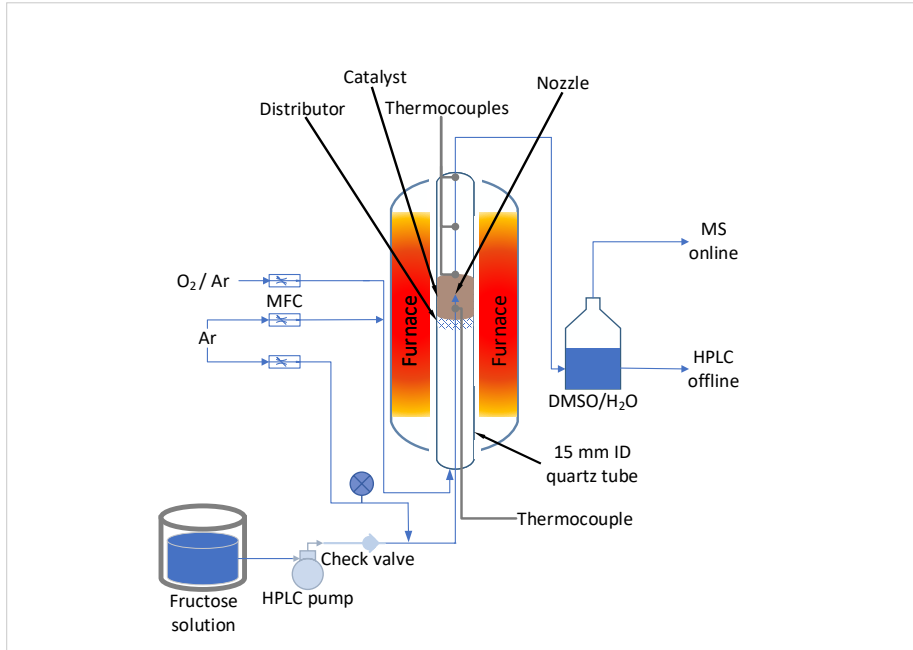


Figure 2: A nozzle atomizes the fructose solution directly into the catalytic bed. A DMSO/H<sub>2</sub>O quench traps the products and an HPLC analyzes the trend. An online MS monitored non-condensable gases.

was the internal standard for the HPLC analysis. At the end of each experiment we cleaned the exit line with 5 mL of water and analyzed this sample.

Product selectivity,  $S_i$ , is based on a molar balance around each component  $i$ ,  $n_i^{\text{out}}$ :

$$S_i = \frac{\sum_j n_{i,j}^{\text{out}} / \vartheta_{i,j}}{n_{\text{fr}}^{\text{in}} - n_{\text{fr}}^{\text{out}}} \cdot 100 \quad (1)$$

where  $n_{\text{fr}}^{\text{in}}$  and  $n_{\text{fr}}^{\text{out}}$  are the moles of fructose entering and exiting the system and  $\vartheta_i$  is the stoichiometric coefficient for the carbon component of each reaction  $j$ . The median droplet size diameter,  $d_{50}$ , exiting the nozzle of an internal mixing air-assist atomizer is [51]:

$$d_{50} = 20 u_L^{0.5} m_L^{0.1} d_L^{0.1} \sigma^{0.2} \rho_g^{-0.3} \Delta U^{-1.0} \left[ 1 + \frac{m_L}{m_g} \right]^{0.5} \quad (2)$$

where  $u_L$  is the superficial velocity,  $m_L$  and  $m_g$  the mass flow of the liquid and the gas,  $d_L$  the orifice dimension,  $\sigma$  is the surface tension and the  $\Delta U$  the relative velocity between the liquid and the gas.

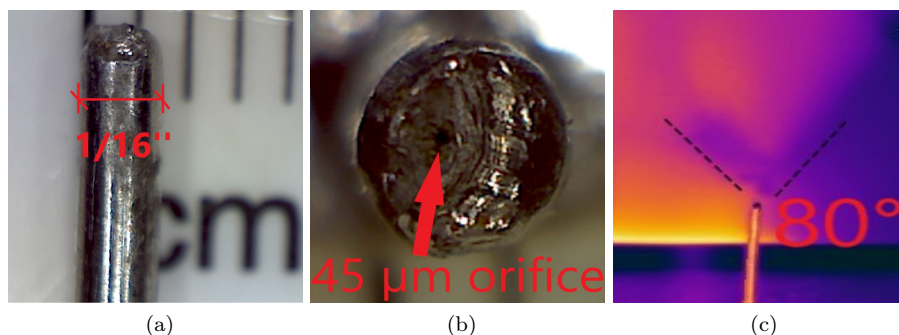


Figure 3: 1/16" (1.59 mm) stainless steel pipe filed at the top to obtain an orifice of 45  $\mu\text{m}$ . The IR camera shows that the atomization and the evaporation at the orifice decreased the temperature at the tip, forming a full cone with an angle of 80°.

### 2.1. Materials

All the reagents are analytical grade without further purification. We acquired D-fructose(99 %) from Alfa Aesar. We purchased 5-hydroxymethyl furfural (99 %), furfural (99 %), 5-hydroxymethyl-2-furancarboxylic acid, 5-formyl-2-furoic acid, 2,5-furandicarboxylic acid (97 %), 2,5-furandicarboxaldehyde (97 %), 5-methyl-2-furaldehyde ( $\geq 98$  %), and tetraammineplatinum(II) nitrate ( $\geq 99.9$  %) and ammonium (para)tungstate hydrate ( $>99.99$  %) from Sigma Aldrich. Air  
 90 Liquide Canada supplied the gases: argon ( $> 99.7$  %), 10.0 % O<sub>2</sub> balance Ar, and a mixture of CO (1.04 %), CO<sub>2</sub> (1.01 %), CH<sub>4</sub> (1.03 %) balance Ar. Huntsman Corporation supplied the titanium dioxide (Hombikat 110100).

### 2.2. Catalyst preparation

We sieved the support powder from 90  $\mu\text{m}$  to 150  $\mu\text{m}$  in diameter. The crystalline phase of the titania was pure anatase. A successive wetness impregnation  
 100 method deposited first WO<sub>3</sub> and then Pt on the TiO<sub>2</sub> support. Initially we determined the total pore volume by dropwise addition of water. Ammonium paratungstate dissolved in a volume of water equivalent to the pore volume of the support. A rotary evaporator operating at 100 rpm for 3 h mixed the active  
 105 phase and support. The catalyst then dried at 70 °C and 300 mbar for 2 h. The powder then calcined in a furnace at 120 °C for 4 h to completely remove traces of water. The furnace then ramped temperature at 2.5 °C min<sup>-1</sup> to 600 °C in air. The powder remained in the furnace at this temperature for 4 h.

### 2.3. Analytical instrumentation

A Philips X'PERT diffractometer generated XRD spectra with a monochromatic Cu-k $\alpha$  beam,  $\lambda = 0.15406$  nm, at 50 kV and 40 mA. It scanned the goniometer axis from 20° to 85°, at a rate of 0.01 ° s<sup>-1</sup>. The crystalline phases were identified with the ICDD database and the Rietveld refinement (X'PERT highscore) gave a semi-quantitative characterization for the phases' weight composition.[52]  
 110

115 The Scherrer approximation defined the average cubic crystallite size:  $D = 0.94\lambda/\beta\cos\theta$ , where  $\lambda$  is the mentioned instrument wavelength,  $\beta$  is the full-width at half-maximum peak height (FWHM, rad), and  $\theta$  is the Bragg angle for the most intense peak (half of the  $2\theta$  position).

120 The FE-SEM-JEOL JSM-7600F scanning electron microscope (SEM) acquired the catalyst images between 5 kV to 30 kV, using secondary and backscattered electrons detectors (secondary electron image —SEI, low secondary electron image —LEI and backscatter image —LABe). The energy dispersive X-ray detector (EDX) mapped the surface of the catalyst and qualitatively quantified the composition and the different phase regions.

A laser diffractometer (Horiba, LA-950) evaluated the particle size distribution (PSD) based on the Mie Theory:

$$D_{4,3} = \frac{\sum d_i^4 \cdot N_i}{\sum d_i^3 \cdot N_i} \quad (3)$$

125 with  $N_i$  as number of particles with diameter  $d_i$ . The particle refractive index was  $2.75 + 0.00i$  (R and Chi parameter below 0.05).

A Quantachrome Autosorb-1 N<sub>2</sub> physisorption instrument recorded the adsorption and desorption isotherms at 77 K. A degasser, operating under vacuum at 300 °C for 6 h, removed the gas adsorbed on the surface [53, 54]. The Brunauer-Emmett-Teller (BET) theory regress the specific surface area at  $P/P_0$  0.05 to 0.3. The instrument estimated the mesopore size distribution over the desorption branch ( $P/P_0$  0.15-0.995), based on the Barrett-Joyner-Hallender (BJH) theory. The total pore volume is evaluated at the maximum filling pressure ( $P/P_0$  0.995), considering all pores with a diameter smaller than 300 nm.

135 A LECO CS744 CHN analyzer measured carbon build up on the catalyst surface after each experiment. An internal balance measured the sample weight loss, when heated above 1000 °C in air. A further CO trap converted the remaining carbon monoxide to CO<sub>2</sub>.

140 A Varian ProStar 325 HPLC, equipped with a UV detector at 260 nm, quantified species concentration of the liquid samples. A MetaCarb 87H column, kept at 60 °C, separated the compounds. The pump flowed a 0.05 N aqueous H<sub>2</sub>SO<sub>4</sub> solution at 0.35 mL min<sup>-1</sup>. Each analysis lasted 70 min to ensure the products separation.

### 3. Results and discussion

#### 145 3.1. Catalyst characterization

##### 3.1.1. Fluidization and particle size distribution

Geldart classified particles into 4 categories based on the catalyst diameter and the differential of the particle density and the gas density [55]. Geldart group A powders are best suited for catalytic fluidized beds with diameters (150  $d_{50}$ ) on the order of 70  $\mu\text{m}$ . Based on the Horiba LA-950, the average spherical particle diameter of fresh catalyst increased from 85  $\mu\text{m}$  to 95  $\mu\text{m}$  (Figure 4). Coke covered the surface (SEM-EDX) and increased the average particle



Table 1: Variation of the catalyst physical characteristics after the reaction

Property	Fresh	Used
$d_{50}$ , $\mu\text{m}$	85	95
SA, $\text{m g}^{-2}$	63	63
Pore volume, $\text{mL g}^{-1}$	0.18	
$u_{\text{mf}}$ , $\text{mm s}^{-1}$	8	
$\rho_{\text{bulk}}$ , $\text{kg m}^{-3}$	770	
Attrition resistance, $\text{mg h}^{-1}$	5.4	5.4

diameter by  $10 \mu\text{m}$ . The bulk density was  $770 \text{kg m}^{-3}$ , so that we classify it as a group A powder.

155 The minimum fluidization velocity,  $u_{\text{mf}}$ , with 3 g of catalyst in the reactor was  $8 \text{mm s}^{-1}$ . Catalyst attrition resistance is a major concern for fluidized beds particularly with high velocity jets where particles collide and fragments or cleaves surface asperities. To prevent this phenomena we opted for the catalyst synthesis by incipient wetness impregnation, which minimizes surface defects and thus asperities. We tested the attrition rate in an air jet mill according to the ASTM 5757 [56]. The high velocity simulates the mechanical stress coming from the nozzle and the distributor. A filtered vessel collected the elutriated fines after 24 h. The catalyst attrits at  $5.4 \text{mg h}^{-1}$ , which is well within commercial practice [57].

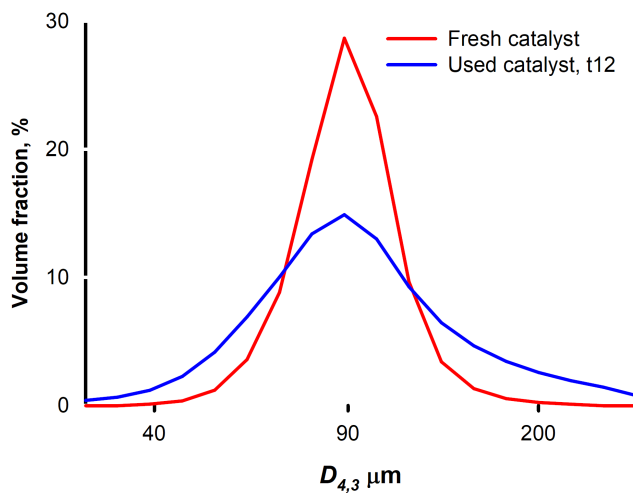


Figure 4: Catalyst particle size distribution in logarithmic scale. Coke deposits broadened the peak and increased the average.

Table 2:  $D$  crystallite size (standard deviation among Pt signals); BET surface area by nitrogen physisorption, results are within 3 % precision (95 % variance);  $\phi$  pore volume;  $\Delta_{dV(d)}$  BJH  $dV(d)$  mesopore median; Coke carbon content (0.05 % precision, 95 % variance).

$\text{WO}_3/\text{TiO}_2$	$D$ nm	BET $\text{m}^2 \text{g}^{-1}$	$\phi$ $\text{mL g}^{-1}$	$\Delta_{dV(d)}$ nm	Coke %
Fresh 0.5 % Pt	52(7)	63	0.183	9.6	na
Fresh 1.5 % Pt	88(2)	63	0.183	9.6	na
Used, t12, 1.5 % Pt	60(10)	63	0.183	9.6	48

### 165 3.1.2. XRD

We analyzed the calcined catalyst before reaction with a mass fraction of 5 %  $\text{WO}_3$  on  $\text{TiO}_2$  and 0.5 % Pt or 1.5 % Pt . We characterized the catalyst at the end of experiment t12 (1.5 % Pt), which had the most coke. XRD analysis detected two crystalline phases: anatase for the titania (ref: 96-900-9087) and platinum (ref: 96-101-1114) while EDX confirmed the presence of W since it was below the XRD detection limit [49]. The titania support maintained a tetragonal structure during calcination and reaction. The platinum presented a cubic structure, with a submicron crystallinity, which increased with Pt loading and decreased due to the coke deposition during the reaction. SEM confirmed the results, providing images of crystals with several hundred nanometers size and a round-prismatic shape. Each crystal contained several crystallites, growing in different directions (Figure 9). At 50 kV, the X-ray penetrated the catalyst down to 35  $\mu\text{m}$  (Pott’s equation) [58]: this surface analysis overestimated the Pt fraction with respect the  $\text{TiO}_2$  support. As coke builds up, the intensity of the Pt signals decrease and broaden (Table 2). During calcination,  $\text{WO}_3$  precursor penetrated the titania lattice thereby reducing the tungsten signal. Calcination at 600 °C was low enough to minimize phase segregation and so the  $\text{WO}_3$  remained amorphous. A weak, unidentified peak emerged at 31.6° after reaction. Reaction conditions may have crystallized part of the amorphous  $\text{WO}_3$  in the mesoporous titania structure however, SEM-EDX could not confirm  $\text{WO}_3$  crystals on the surface of the catalyst but  $\text{N}_2$  physisorption detected a decrease in pore size after reaction. The small crystallite size (30 nm) and the strong chemical interaction with the surrounding environment (coke and titania) shift the signal.

### 190 3.1.3. BET

The  $\text{TiO}_2$  support and tungsten salt precursor contribute most to the specific surface area (SSA), pore size distribution and pore volume (PV) of the catalyst after calcination (Figure 6) [49]. Calcined catalyst has a type IV isotherm and an  $H2$  hysteresis loop: mesoporous structure with a narrow distribution of pore necks [60, 54]. A mass fraction of 1.5 % Pt decreased the SSA with respect to calcined  $\text{WO}_3/\text{TiO}_2$  catalyst. EDX images show Pt on the surface but not in the interior so the drop in SSA and PV is due to pore-blocking. Pt obstructed pores smaller than 10 nm, which increased the characteristic pore median ( $dS(d)$ ) by

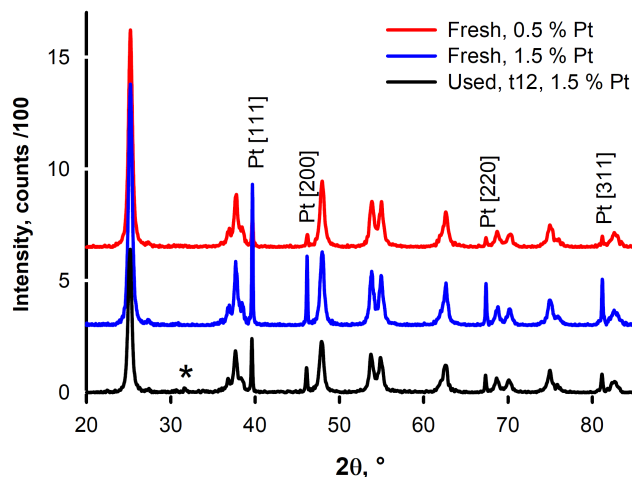


Figure 5: Stacked spectra recorded with the same conditions and smoothed with an 11 points cubic function, Cu- $k\alpha$  sidebands were removed: coke deposits on the used sample reduced the signal to noise ratio. Four sharp Pt signals ( $39.6^\circ$ ,  $46.0^\circ$ ,  $67.4^\circ$ ,  $81.2^\circ$ ) and their respective planes  $[hkl]$  have been identified. The remaining peaks belong to the titania support (anatase) [59].

1 nm. The “t12” catalyst has a type I-IV isotherm and an open  $H4$  hysteresis: a  
 200 microporous network developed as coke partially filled the internal mesoporous  
 structure. Despite coke deposits, furanic selectivity improved with time. The  
 SSA increased with respect to calcined catalyst, suggesting a selective coke  
 deposit. This phenomenon decreased the reagent and product degradation,  
 despite the pore size dropping from 11.0 nm to 0.7 nm) and the lower pore volume  
 205 (Table 2). The BJH surface distribution shrunk in the mesopore region. The  
 quenched solid state functional theory (QSDFT) for SSA deviated less than 5%  
 from the BET SSA.

#### 3.1.4. Field Emission Scanning Electron Microscopy (FE-SEM)/EDX

The tungsten oxide was homogeneously dispersed on the titania support.  
 210 Pt crystals were poorly dispersed on the surface as SEM images show regions  
 with bright spots with Pt particles (Figure 7). Furthermore, some particles  
 have much more Pt than others. The Pt submicron crystals were 250  $\mu\text{m}$  on  
 average (Figure 8). After reaction, Pt particles formed agglomerate with several  
 hundred crystals but the powder remained free flowing. Only on the sparger tip  
 215 circumference did powder agglomerate [46].

An EDX scan at 20 kV of the catalyst surface to a depth of 10  $\mu\text{m}$  confirmed  
 that W covered the surface uniformly. On the contrary, Pt forms submicron  
 crystals rather than forming a monolayer on the surface or in the interior.  
 Titanium-oxygen molar ratios were coherent with the  $\text{TiO}_2$  composition. Pt  
 220 was only in the metallic form since the EDX oxygen image showed dark spots  
 corresponding to the Pt crystals (Figure 10).

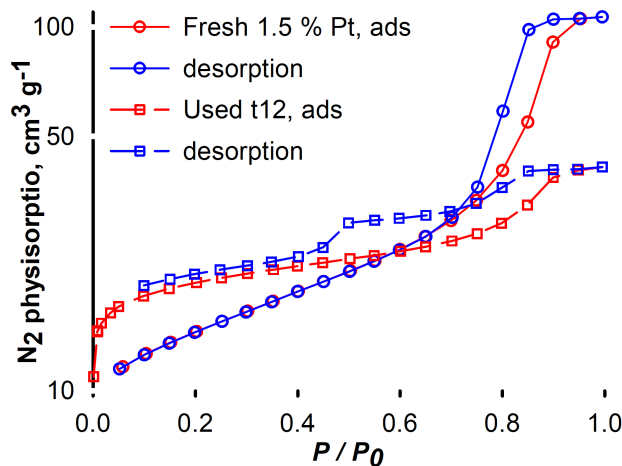


Figure 6: Nitrogen physisorption isotherms. The used catalyst loses the microporous fraction and the total pore volume decreases as a consequence. Carbon obstructing the mouth of the micropores accounts for the large reduction at  $P/P_0 > 0.7$ .

We crushed used catalyst and the SEM images of the chunks showed no coke in the interior. As much as (20  $\mu\text{m}$ ) of coke covered some of the particles but most of it was homogeneously distributed on the surface (Figure 10). Clearly, since the carbon coverage was uniform  $\text{WO}_3$  rather than Pt initiated the growth of the coke layer. An EDX spectrum on the coke deposit identified a molar composition of 90 % carbon and 10 % oxygen.

### 3.2. Internal-mixing two-fluid nozzle

Operating the fluidized bed was problematic due to frequent interruptions in the fluid flow due to solids build up in the sparger. The large surface to volume ratio of the sparger was a contributing factor as the water would evaporate in the tube and the fructose would then crystallize. We injected Ar at  $50 \text{ mL min}^{-1}$  to reduce the residence time of the solution in the tube and improve the effervescent spray of the liquid. The gas and fluid first mix at the t-junction below the sparger tip. We reduce the internal diameter of the top part of a stainless steel pipe of 1.5875 mm OD and 0.127 mm ID (Figure 3a) to create a  $45 \mu\text{m} \pm 5 \mu\text{m}$  orifice (Figure 3b), which is a 65 % reduction of the internal diameter. The setup produced a full cone spray with an angle of  $80^\circ \pm 5^\circ$ , measured by infrared camera after heating the nozzle to  $400^\circ\text{C}$ .

Based on Equation 2, the median droplet size was  $5 \mu\text{m}$ , with a Weber number of 7. The gas flow was laminar around the particles ( $N_{\text{Re}} = 11$ ) and at the orifice ( $N_{\text{Re}} = 750$ ). Higher Re and We numbers increase the atomization speed and reduce the droplet diameter. Internal mixing increased the contact between the gas and the liquid producing finer droplets [51].

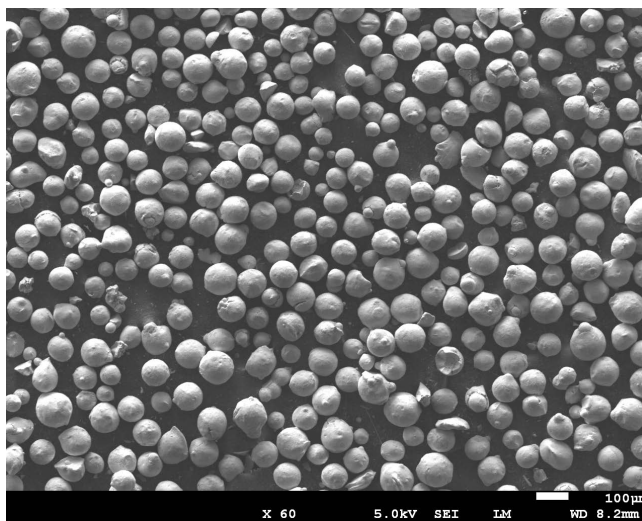


Figure 7: Fresh 1.5 % Pt over  $\text{WO}_3/\text{TiO}_2$  particles. The LABe detector enhanced the signal from heavy elements and the Pt crystals appeared as bright white spots [61].

### 245 3.3. Screening test and full factorial design

A Plackett-Burman screening design assessed the influence of six factors: temperature (150 °C and 300 °C),  $\text{O}_2$ :fructose molar ratio (2:1 and 20:1), catalyst mass (2.5 g and 5 g), Pt loading (0.5 % and 1.5 %), feed flowrate (50  $\mu\text{L min}^{-1}$  and 100  $\mu\text{L min}^{-1}$ ) and feed fructose mass concentration (2.5 % and 5 %). The design comprised 12 experiments.

250 All the tests demonstrated total conversion of fructose and produced coke, COx, and various organic compounds. Some of the fructose degraded along the walls and exit line.

The dehydration reaction was independent of oxygen concentration but it helped control coke build-up on the surface. The two levels of mass of catalyst loaded varied the contact time, while two flowrates modified the weight hour space velocity and the gaseous partial pressure of water.

260 Catalyst loading accounted for most of the variance in the data: furanic products selectivity was greater with less catalyst. The maximum total product selectivity never exceeded 6 %, due to the extreme conditions of the screening test.  $\text{CO}_2$  and CO rose with temperature, reaching 59 % and 4 % at 300 °C, respectively. Furthermore, higher oxygen concentration produced more  $\text{CO}_2$ . HMF, the dehydration product, increased with higher liquid flowrate and lower catalyst loading. Increasing the partial pressure of water increased the catalytic surface saturation, lowering the degradation kinetics. HMF conversion increased with higher contact time. Furfural, the decarbonylation product of HMF (Figure 1), depended only on catalyst loading—it increased with longer contact time. Maximizing the contact time, determined the fructose and the intermediate degradation to coke and COx. HMF hydrodehydrates to 5MF

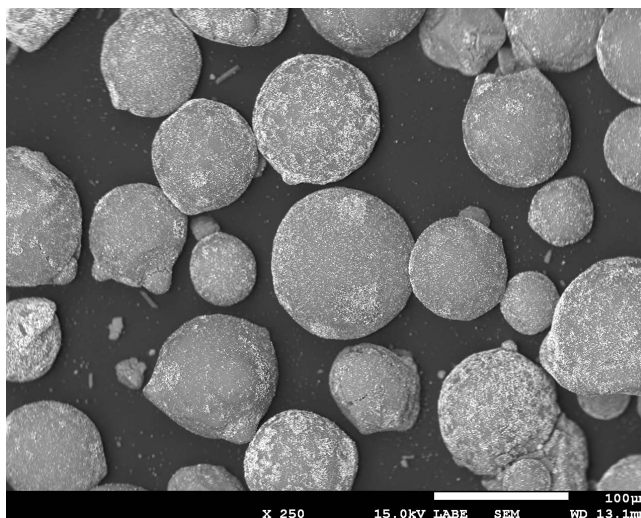


Figure 8: Fresh 1.5 % Pt over  $\text{WO}_3/\text{TiO}_2$  particles. The metallic platinum crystals appeared as multi-facets prisms. Considering their sizes (submicron), the crystallite size of 88 nm (XRD) and the crystal structure of metallic Pt (cubic), several crystallites compose the crystal.

270 (Figure 1). Higher temperature and lower catalyst loading increase selectivity. Furthermore, lower  $\text{O}_2$  concentration reduces the conversion of  $\text{H}_2$  to water, increasing the hydrogenation reaction rate. Increasing the Pt favored hydrogen adsorption, and consequently 5MF.

Oxygen reacts with HMF to HMFCFA and DFF (Figure 1). Oxidation kinetics of the hydroxyl moiety of HMF is faster than the conversion of the aldehydic functional group. DFF only reached a maximum selectivity of 1 %, while HMFCFA never exceeded 0.05 %. Lower catalyst loading and higher temperature increased the selectivity, which is consistent for a high activation energy for HMF oxidation. Furthermore, as for all the furanic compounds, lower catalyst loading reduced the contact time and the degradation process. A further oxidation of HMFCFA and DFF led to FDCA. The amount of catalyst tested was high, leading to elevated contact time and increasing the degradation.

We executed a full factorial design including three levels for temperature (300 °C, 350 °C, and 400 °C) and  $\text{O}_2$  content (0.5, 1 and 10 molar ratio with fructose) and two levels of catalyst loading (1.5 g and 3 g). We kept Pt loading (1.5 %) constant, increasing the liquid flowrate ( $300 \mu\text{L min}^{-1}$ ) and keeping the fructose mass percentage in the feed at 2 % (Table 3).

The contact time,  $\tau$ , between the fructose injected and the catalyst varied between 0.3s to 0.4s and fructose conversion was complete for all experiments (Table 3). The carbon balance was between 57 % to 97 %. Carbon losses were due to product degradation on the reactor wall or inside the exit line. The catalyst becomes increasingly selective with time and this induction time can exceed 2 h so the reported selectivities are pessimistic since they are calculated based on the 3 h from when the pump started. The mass balance of several tests

Table 3: Fructose oxidehydration full factorial design of experiments over 1.5 % Pt-WO<sub>3</sub>/TiO<sub>2</sub>. Factors include catalyst loading (2 levels), temperature (3 levels), and O<sub>2</sub>:fructose molar ratio (3 levels). The selectivities are calculated from time 0 min to 180 min. HMF: 5-hydroxymethyl furfural; FUR: furfural; 5MF: 5-methyl furfural; DFF: diformyl furan.

Exp #	Cat g	$T$ °C	O <sub>2</sub> /fruct	$S_{CO_2}$ %	$S_{CO}$ %	$S_{CH_4}$ %	$S_{Coke}$ %	$S_{HMF}$ %	$S_{FUR}$ %	$S_{5MF}$ %	$S_{DFF}$ %
1	3	300	0.5	6	6	9	8	0	5	3	1
2	3	400	1	12	10	5	10	4	5	1	1
3	1.5	300	10	20	4	17	6	6	4	0	1
4	1.5	400	1	2	3	1	12	9	3	0	0
5	3	350	10	4	3	4	55	3	2	1	1
6	3	300	1	3	12	2	43	3	1	0	0
7	1.5	350	10	0	2	0	21	1	1	0	0
8	3	350	0.5	8	5	4	54	0	5	4	3
9	1.5	300	0.5	2	0	1	13	0	1	0	0
10	1.5	300	1	4	2	3	36	5	6	1	1
11	3	350	1	12	6	5	57	1	5	4	3
12	1.5	350	1	7	5	5	49	11	6	1	2
13	1.5	350	0.5	4	3	4	31	12	6	1	1
14	1.5	400	1	7	3	5	48	7	3	1	3
15	3	400	10	47	1	17	43	0	0	0	0
16	3	300	10	41	1	15	66	1	2	0	1
17	3	400	0.5	4	2	2	24	1	9	6	2
18	1.5	400	10	11	8	3	20	0	7	4	2

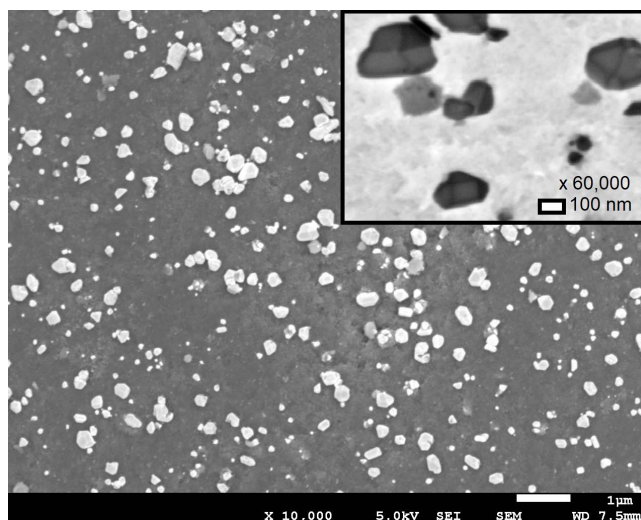


Figure 9: Used “t12” catalyst’s surface. Shiny “metallic-lookalike” coke chunks were dispersed around the spherical catalyst particles after mechanical breakage. Some particles broke as well.

295 were less than 50 % so we have ignored these tests while assessing the impacts of the various factors. The sum of the selective oxidation products—HMF, furfural, 5-methyl furfural, and DFF—reached 20 %. The highest yield of DFF was only 3 % but HMF, the first step of the process, reached 12 %. According to a power-law regression model, the furanic’s concentration increases linearly with  
 300 temperature but decreases with the square root of mass of catalyst and decreases to a lower power with the oxygen:fructose ratio—feeding more oxygen reduces the productivity (Figure 11). The correlation explains 63 % of the variance in the data but excludes experiments for which the mass balance closure is less than 50 %. The reason relates to the temperature, which was too low to react.

The  $\text{CO}_2$  selectivity reached 20 % while the maximum CO selectivity and  $\text{CH}_4$  selectivity were 12 % and 17 %, respectively. The concentration of  $\text{CO}_2$  was highly correlated with  $\text{CH}_4$ . Excluding experimental data for which the mass balance closed to below 50 %

$$\text{CH}_4 = 1.2 \frac{\text{CO}_2}{W} \quad R^2 > 0.9 \quad (4)$$

305 where  $W$  is the mass of catalyst (Figure 12). Data  $\text{CO}_2$  selectivity was essentially independent of temperature; it increased with the square-root of the  $\text{O}_2$ :fructose ratio, and increased more than linearly with the mass of catalyst. Coke formation is related to the decomposition of the feed or the products on the catalyst and built up in all experiments and agglomerated.



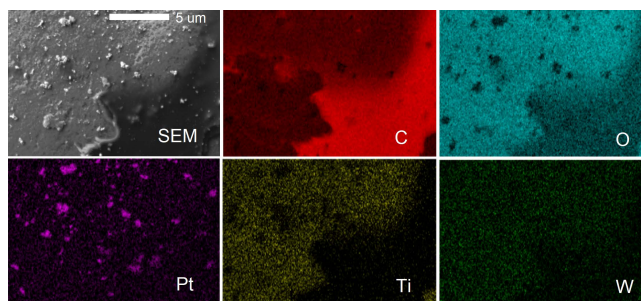


Figure 10: SEM and EDS mapping of the used “t12” catalyst’s surface. Carbon (C, red) partially covered the surface and suppressed the underlying elements’ signals. Oxygen (O, blue) was predominant were titanium was also present (Ti, yellow), less were carbon was present and absent were platinum was present (Pt, violet). Tungsten (W, green) was homogeneously distributed along with titanium.

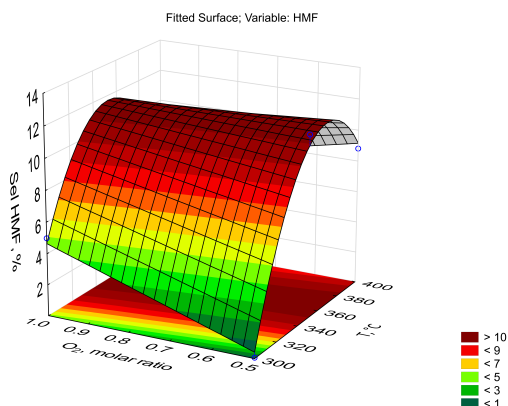


Figure 11: Surface chart of HMF selectivity with 1.5 g catalyst loading.

### 310 3.4. HMF to DFF

We investigated the oxidation of HMF to DFF at four temperatures between 250 °C to 400 °C and two catalyst loading, 1.5 g and 5 g, maintaining the O<sub>2</sub>:HMF molar ratio of 2 (Table 4). Higher catalyst loading reacted all the HMF at the expense of DFF selectivity which approached at most 4%. On the other hand, at low catalyst loading and 350 °C or 400 °C DFF selectivity was 26 % and 16 %, respectively. Conversion dropped to 86 % at 250 °C and DFF selectivity increased to 42 %.

5MF, the main by-product of the reaction, is mainly controlled by temperature and catalyst inventory. In fact, at higher contact time, the selectivity dropped to 2 %, while decreasing the temperature from 400 °C to 200 °C, the selectivity increased from 12 % to a maximum of 18 %. Furfural, the other main by-product, remained almost stable around 6 % for all the reactions with lowest amount of catalyst, but ranged was 1 % with 5 g of catalyst Coke built up on

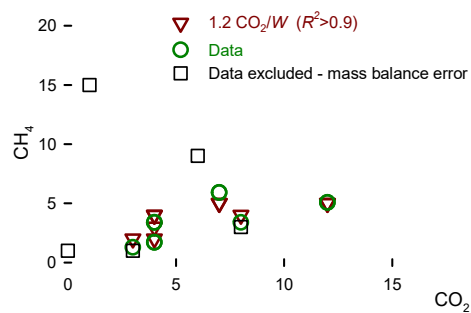


Figure 12: CH<sub>4</sub> selectivity versus CO<sub>2</sub> selectivity. Data from 5 experiments were excluded as the mass balance closed to less than 5% (open square symbols).

Table 4: Higher contact time increase the degradation kinetic. Decreasing the temperature decreases the conversion but raise the DFF selectivity. The O<sub>2</sub>:HMF ratio was 2 for all experiments.

Mass g	$T$ °C	Conversion %	$S_{\text{CO}_2}$ %	$S_{\text{CO}}$ %	$S_{\text{FUR}}$ %	$S_{5\text{MF}}$ %	$S_{\text{DFF}}$ %
1.5	350	100	6	6	9	11	26
5	350	100	4	6	0	1	0
1.5	400	100	23	6	4	12	16
5	400	100	11	5	1	2	4
1.5	300	92	3	28	1	11	15
1.5	250	86	15	18	6	18	42

the catalyst, but was insensitive to either temperature or catalyst loading.

325 CO and CO<sub>2</sub> the selectivity varied considerably with both temperature and  
catalyst loading. At low temperature and low catalyst loading, CO was higher  
than CO<sub>2</sub>, but increasing the two variables, the ratio became 1:1 and with a  
further increase CO<sub>2</sub> selectivity became higher than that of CO. The higher  
330 contact time increased the degradation of the molecules and carbon oxide selec-  
tivity increased with temperature.

#### 4. Conclusions

Gas phase fructose oxidehydration is a new pathway to platform chemicals  
from organic feedstocks. It avoids organic solvents, decreases reaction time  
to fractions of a second, and facilitate product separation. Fructose first de-  
335 hydrates to HMF followed by tandem reactions to furfural, 5-MF, and DFF.  
Other undesirable products are CO, CO<sub>2</sub>, CH<sub>4</sub>, and coke. The ceCH<sub>4</sub> is lin-  
early correlated with CO<sub>2</sub> while the selectivity to coke was highest among the  
products detected. Generally, the mass balance was greater than 50 % but for  
5 of the 18 experiments in the full factorial design it was less than this. HMF  
340 selectivity from fructose reached 12 % at 350 °C. Other partial oxidatio product  
selectivity were less than 7 %. Even shorter contact times are required to im-  
prove selectivity and reduce conversion. Since the catalyst induction time was  
on the order of 2 h (the catalyst continued to activate), the product selectivities  
are certainly higher. Coke built up on the catalytic surface, agglomerating the  
345 catalyst but also covered the strongest acid sites, enhancing the selectivity to  
the furanic compounds. Feeding HMF rather than fructose demonstrated that  
lower temperatures are required to increase the furanic's selectivity.

#### 5. References

##### References

- 350 [1] S. Macrelli, J. Mogensen, G. Zacchi, Techno economic evaluation of 2nd  
generation bioethanol production from sugar cane bagasse and leaves inte-  
grated with the sugar based ethanol process, *Biotechnology for Biofuels* 5  
(2012) 22. doi:10.1186/1754-6834-5-22.
- [2] A. A. Rosatella, S. P. Simeonov, R. F. M. Frade, C. A. M. Afonso, 5-  
355 Hydroxymethylfurfural (HMF) as a building block platform: Biological  
properties, synthesis and synthetic applications, *Green Chemistry* 13 (4)  
(2011) 754. doi:10.1039/c0gc00401d.  
URL <http://xlink.rsc.org/?DOI=c0gc00401d>
- [3] E. Taarning, C. M. Osmundsen, X. Yang, B. Voss, S. I. Andersen, C. H.  
360 Christensen, Zeolite-catalyzed biomass conversion to fuels and chemicals,  
*Energy and Environmental Science* 4 (2011) 793–804. doi:DOI:10.1039/  
C004518G.

- [4] N. Ly, K. Al-Shamery, C. E. Chan-Thaw, L. Prati, P. Carniti, A. Gervasini, Impact of Support Oxide Acidity in Pt-Catalyzed HMF Hydrogenation in Alcoholic Medium, *Catalysis Letters* 147 (2) (2017) 345–359. doi:10.1007/s10562-016-1945-9. 365
- [5] J. Tuteja, H. Choudhary, S. Nishimura, K. Ebitani, Direct synthesis of 1,6-hexanediol from HMF over a heterogeneous Pd/ZrP catalyst using formic acid as hydrogen source, *ChemSusChem* 7 (1) (2014) 96–100. doi:10.1002/cssc.201300832. 370
- [6] C. Lucarelli, S. Galli, A. Maspero, A. Cimino, C. Bandinelli, A. Lolli, J. Velasquez Ochoa, A. Vaccari, F. Cavani, S. Albonetti, Adsorbent-Adsorbate Interactions in the Oxidation of HMF Catalyzed by Ni-Based MOFs: A DRIFT and FT-IR Insight, *Journal of Physical Chemistry C* 120 (28) (2016) 15310–15321. doi:10.1021/acs.jpcc.6b05428. 375
- [7] F. L. Grasset, B. Katryniok, S. Paul, V. Nardello-Rataj, M. Pera-Titus, J.-M. Clacens, F. De Campo, F. Dumeignil, Selective oxidation of 5-hydroxymethylfurfural to 2,5-diformylfuran over intercalated vanadium phosphate oxides, *RSC Advances* 3 (25) (2013) 9942. doi:10.1039/c3ra41890a. 380  
URL <http://xlink.rsc.org/?DOI=c3ra41890a>
- [8] N. T. Le, P. Lakshmanan, K. Cho, Y. Han, H. Kim, Selective oxidation of 5-hydroxymethyl-2-furfural into 2,5-diformylfuran over VO<sub>2</sub><sup>+</sup> and Cu<sup>2+</sup> ions immobilized on sulfonated carbon catalysts, *Applied Catalysis A: General* 464-465 (2013) 305–312. doi:10.1016/j.apcata.2013.06.002. 385  
URL <http://dx.doi.org/10.1016/j.apcata.2013.06.002>
- [9] X. Wan, C. Zhou, J. Chen, W. Deng, Q. Zhang, Y. Yang, Y. Wang, Base-free aerobic oxidation of 5-hydroxymethyl-furfural to 2,5-furandicarboxylic acid in water catalyzed by functionalized carbon nanotube-supported au-pd alloy nanoparticles, *ACS Catalysis* 4 (7) (2014) 2175–2185. doi:10.1021/cs5003096. 390
- [10] Z. Zhang, J. Zhen, B. Liu, K. Lv, K. Deng, Selective aerobic oxidation of the biomass-derived precursor 5-hydroxymethylfurfural to 2,5-furandicarboxylic acid under mild conditions over a magnetic palladium nanocatalyst, *Green Chem.* 17 (2) (2015) 1308–1317. doi:10.1039/C4GC01833H. 395  
URL <http://xlink.rsc.org/?DOI=C4GC01833H>
- [11] Avantium, YXY technology for bio-based packaging (2018).  
URL <https://www.synvina.com/technology/process>
- [12] N. van Strien, S. Rautiainen, M. Asikainen, D. A. Thomas, J. Linnekoski, K. Niemelä, A. Harlin, A unique pathway to platform chemicals: aldaric acids as stable intermediates for the synthesis of furandicarboxylic acid esters, *Green Chemistry* 22 (23) (2020) 8271–8277. 400

- 405 [13] V. Choudhary, S. H. Mushrif, C. Ho, A. Anderko, V. Nikolakis, N. S. Marinkovic, A. I. Frenkel, S. I. Sandler, D. G. Vlachos, Insights into the interplay of Lewis and Brønsted acid catalysts in glucose and fructose conversion to 5-(hydroxymethyl) furfural and levulinic acid in aqueous media, *Journal of the American Chemical Society* 135 (10) (2013) 3997–4006. doi:10.1021/ja3122763.
- 410 [14] C. Antonetti, M. Melloni, D. Licursi, S. Fulignati, E. Ribechini, S. Rivas, J. C. Parajó, F. Cavani, A. M. Raspolli Galletti, Microwave-assisted dehydration of fructose and inulin to HMF catalyzed by niobium and zirconium phosphate catalysts, *Applied Catalysis B: Environmental* 206 (2017) 364–377. doi:10.1016/j.apcatb.2017.01.056.  
415 URL <http://dx.doi.org/10.1016/j.apcatb.2017.01.056>
- [15] Y. Li, H. Liu, C. Song, X. Gu, H. Li, W. Zhu, S. Yin, C. Han, The dehydration of fructose to 5-hydroxymethylfurfural efficiently catalyzed by acidic ion-exchange resin in ionic liquid, *Bioresource Technology* 133 (2013) 347–353. doi:10.1016/j.biortech.2013.01.038.  
420 URL <http://dx.doi.org/10.1016/j.biortech.2013.01.038>
- [16] H. Zhao, J. E. Holladay, H. Brown, Z. C. Zhang, Metal chlorides in ionic liquid solvents convert sugars to 5-hydroxymethylfurfural, *Science* 316 (5831) (2007) 1597–1600. doi:10.1126/science.1141199.
- 425 [17] L. Cao, I. K. Yu, S. S. Chen, D. C. Tsang, L. Wang, X. Xiong, S. Zhang, Y. S. Ok, E. E. Kwon, H. Song, C. S. Poon, Production of 5-hydroxymethylfurfural from starch-rich food waste catalyzed by sulfonated biochar, *Bioresource Technology* 252 (October 2017) (2018) 76–82. doi:10.1016/j.biortech.2017.12.098.  
URL <https://doi.org/10.1016/j.biortech.2017.12.098>
- 430 [18] M. Bicker, D. Kaiser, L. Ott, H. Vogel, Dehydration of D-fructose to hydroxymethylfurfural in sub- and supercritical fluids, *Journal of Supercritical Fluids* 36 (2) (2005) 118–126. doi:10.1016/j.supflu.2005.04.004.
- 435 [19] J. K. C. N. Agutaya, R. Inoue, S. S. Vin Tsie, A. T. Quitain, J. de la Pena-Garcia, H. Perez-Sanchez, M. Sasaki, T. Kida, Metal-free synthesis of hmf from glucose using the supercritical co<sub>2</sub>-subcritical h<sub>2</sub>o-isopropanol system, *Industrial & Engineering Chemistry Research* 59 (38) (2020) 16527–16538.
- 440 [20] S. K. Patil, C. R. Lund, Formation and growth of humins via aldol addition and condensation during acid-catalyzed conversion of 5-hydroxymethylfurfural, *Energy and Fuels* 25 (10) (2011) 4745–4755. doi:10.1021/ef2010157.
- [21] R. Li, Q. Lin, Y. Wang, W. Yang, X. Liu, W. Li, X. Wang, X. Wang, C. Liu, J. Ren, Brønsted acid-driven conversion of glucose to xylose, arabinose and

- formic acid via selective c–c cleavage, *Applied Catalysis B: Environmental* 286 (2021) 119862.
- 445 [22] A. Al Ghatta, X. Zhou, G. Casarano, J. D. Wilton-Ely, J. P. Hallett, Characterization and valorization of humins produced by hmf degradation in ionic liquids: A valuable carbonaceous material for antimony removal, *ACS Sustainable Chemistry & Engineering* (2021).
- 450 [23] K. Sun, Y. Shao, Q. Li, L. Zhang, Z. Ye, D. Dong, S. Zhang, Y. Wang, X. Li, X. Hu, Importance of the synergistic effects between cobalt sulfate and tetrahydrofuran for selective production of 5-hydroxymethylfurfural from carbohydrates, *Catalysis Science & Technology* 10 (7) (2020) 2293–2302.
- 455 [24] Y. J. Pagán-Torres, T. Wang, J. M. R. Gallo, B. H. Shanks, J. A. Dumesic, Production of 5-hydroxymethylfurfural from glucose using a combination of lewis and brønsted acid catalysts in water in a biphasic reactor with an alkylphenol solvent, *ACS Catalysis* 2 (6) (2012) 930–934. doi:10.1021/cs300192z.
- 460 [25] J. N. Chheda, Y. Román-Leshkov, J. A. Dumesic, Production of 5-hydroxymethylfurfural and furfural by dehydration of biomass-derived mono- and poly-saccharides, *Green Chem.* 9 (4) (2007) 342–350. doi:10.1039/B611568C.  
URL <http://xlink.rsc.org/?DOI=B611568C>
- 465 [26] E. Taarning, I. Sádaba, P. R. Jensen, S. Meier, Discovery and exploration of the efficient acyclic dehydration of hexoses in dmsO/water, *ChemSusChem* 12 (2019) 5086–5091.
- [27] S. Hu, Z. Zhang, Y. Zhou, J. Song, H. Fan, B. Han, Direct conversion of inulin to 5-hydroxymethylfurfural in biorenewable ionic liquids, *Green Chemistry* 11 (6) (2009) 873. doi:10.1039/b822328a.  
470 URL <http://xlink.rsc.org/?DOI=b822328a>
- [28] B. Liu, Y. Ren, Z. Zhang, Aerobic oxidation of 5-hydroxymethylfurfural into 2,5-furandicarboxylic acid in water under mild conditions, *Green Chem.* 17 (3) (2015) 1610–1617. doi:10.1039/C4GC02019G.  
475 URL <http://xlink.rsc.org/?DOI=C4GC02019G>
- [29] G. Yi, S. P. Teong, Y. Zhang, Base-free conversion of 5-hydroxymethylfurfural to 2,5-furandicarboxylic acid over a Ru/C catalyst, *Green Chem.* 18 (4) (2016) 979–983. doi:10.1039/C5GC01584G.  
URL <http://xlink.rsc.org/?DOI=C5GC01584G>
- 480 [30] X. Liu, M. Zhang, Z. Li, Coo x-mc (mc= mesoporous carbon) for highly efficient oxidation of 5-hydroxymethylfurfural (5-hmf) to 2, 5-furandicarboxylic acid (fdca), *ACS Sustainable Chemistry & Engineering* 8 (12) (2020) 4801–4808.

- 485 [31] C. Megías-Sayago, A. Lolli, D. Bonincontro, A. Penkova, S. Albonetti,  
F. Cavani, J. A. Odriozola, S. Ivanova, Effect of gold particles size over  
au/c catalyst selectivity in hmf oxidation reaction, *ChemCatChem* 12 (4)  
(2020) 1177–1183.
- [32] F. Koopman, N. Wierckx, J. H. D. Winde, H. J. Ruijssenaars, *Bioresource*  
490 *Technology* Efficient whole-cell biotransformation of 5-(hydroxymethyl)  
furfural into FDCA , 2 , 5-furandicarboxylic acid, *Bioresource Technol-*  
*ogy* 101 (16) (2010) 6291–6296. doi:10.1016/j.biortech.2010.03.050.  
URL <http://dx.doi.org/10.1016/j.biortech.2010.03.050>
- [33] H. Yuan, J. Li, H. dong Shin, G. Du, J. Chen, Z. Shi, L. Liu, Im-  
495 proved production of 2,5-furandicarboxylic acid by overexpression of 5-  
hydroxymethylfurfural oxidase and 5-hydroxymethylfurfural/furfural oxi-  
doreductase in *Raoultella ornithinolytica* BF60, *Bioresource Technology*  
247 (August 2017) (2018) 1184–1188. doi:10.1016/j.biortech.2017.  
08.166.  
URL <http://dx.doi.org/10.1016/j.biortech.2017.08.166>
- 500 [34] M. M. Cajnko, U. Novak, M. Grilc, B. Likozar, Enzymatic conversion re-  
actions of 5-hydroxymethylfurfural (hmf) to bio-based 2, 5-diformylfuran  
(dff) and 2, 5-furandicarboxylic acid (fdca) with air: mechanisms, pathways  
and synthesis selectivity, *Biotechnology for biofuels* 13 (2020) 1–11.
- [35] Y. Leshkov, J. N. Chheda, J. A. Dumesic, Phase modifiers promote effi-  
505 cient production of hydroxymethylfurfural from fructose, *Science* 312 (5782)  
(2006) 1933–1937. doi:10.1126/science.1126337.
- [36] G. Shen, B. Andrioletti, Y. Queneau, Furfural and 5-(hydroxymethyl) fur-  
fural (hmf): two pivotal intermediates for bio-based chemistry, *Current*  
*Opinion in Green and Sustainable Chemistry* (2020) 100384.
- 510 [37] A. H. Motagamwala, W. Won, C. Sener, D. M. Alonso, C. T. Maravelias,  
J. A. Dumesic, Toward biomass-derived renewable plastics: Production of  
2,5-furandicarboxylic acid from fructose, *Science Advances* 4 (1) (2018)  
eaap9722. doi:10.1126/sciadv.aap9722.  
URL <http://advances.sciencemag.org/lookup/doi/10.1126/sciadv.aap9722>
- 515 [38] D. Yan, G. Wang, K. Gao, X. Lu, J. Xin, S. Zhang, One-Pot Synthesis of  
2,5-Furandicarboxylic Acid from Fructose in Ionic Liquids, *Industrial and*  
*Engineering Chemistry Research* 57 (6) (2018) 1851–1858. doi:10.1021/  
acs.iecr.7b04947.
- 520 [39] T. Kan, V. Strezov, T. J. Evans, Lignocellulosic biomass pyrolysis: A re-  
view of product properties and effects of pyrolysis parameters, *Renewable*  
*and Sustainable Energy Reviews* 57 (2016) 126–1140. doi:10.1016/j.  
rser.2015.12.185.  
URL <http://dx.doi.org/10.1016/j.rser.2015.12.185>

- 525 [40] C. B. Schandel, M. Høj, C. M. Osmundsen, A. D. Jensen, E. Taarning, Thermal cracking of sugars for the production of glycolaldehyde and other small oxygenates, *ChemSusChem* 13 (4) (2020) 688–692.
- [41] C. B. Schandel, M. Høj, C. M. Osmundsen, M. J. Beier, E. Taarning, A. D. Jensen, Kinetic modeling of gas phase sugar cracking to glycolaldehyde and other oxygenates, *ACS Sustainable Chemistry & Engineering* 9 (1) (2021) 305–311. doi:10.1021/acssuschemeng.0c07232.
- 530 [42] D. K. Shen, S. Gu, Pyrolytic behaviour of cellulose in a fluidized bed reactor, *Cellulose chemistry and technology* 44 (1-3) (2010) 79–87.
- [43] K. J. Wu, C. F. Chang, J. S. Chang, Simultaneous production of biohydrogen and bioethanol with fluidized-bed and packed-bed bioreactors containing immobilized anaerobic sludge, *Process Biochemistry* 42 (7) (2007) 1165–1171. doi:10.1016/j.procbio.2007.05.012.
- 535 [44] C. Z. Liu, F. Wang, F. Ou-Yang, Ethanol fermentation in a magnetically fluidized bed reactor with immobilized *Saccharomyces cerevisiae* in magnetic particles, *Bioresource Technology* 100 (2) (2009) 878–882. doi:10.1016/j.biortech.2008.07.016. URL <http://dx.doi.org/10.1016/j.biortech.2008.07.016>
- [45] H. J. S. Lopes, L. R. Ramos, C. A. de Menezes, E. L. Silva, Simultaneous hydrogen and ethanol production in a thermophilic afbr: a comparative approach between cellulosic hydrolysate single fermentation and the fermentation of glucose and xylose as co-substrates, *Cellulose* 27 (5) (2020) 2599–2612.
- 545 [46] T. Ghaznavi, C. Neagoe, G. S. Patience, Partial oxidation of D-xylose to maleic anhydride and acrylic acid over vanadyl pyrophosphate, *Biomass and Bioenergy* 71 (2014) 285–293. doi:10.1016/j.biombioe.2014.09.029. URL <http://dx.doi.org/10.1016/j.biombioe.2014.09.029>
- 550 [47] M. Dalil, D. Carnevali, J. L. Dubois, G. S. Patience, Transient acrolein selectivity and carbon deposition study of glycerol dehydration over  $\text{WO}_3/\text{TiO}_2$  catalyst, *Chemical Engineering Journal* 270 (2015) 557–563. doi:10.1016/j.cej.2015.02.058. URL <http://dx.doi.org/10.1016/j.cej.2015.02.058>
- 555 [48] M. Dalil, D. Carnevali, M. Edake, A. Auroux, J. L. Dubois, G. S. Patience, Gas phase dehydration of glycerol to acrolein: Coke on  $\text{WO}_3/\text{TiO}_2$  reduces by-products, *Journal of Molecular Catalysis A: Chemical* 421 (2016) 146–155. doi:10.1016/j.molcata.2016.05.022. URL <http://dx.doi.org/10.1016/j.molcata.2016.05.022>
- 560 [49] D. Carnevali, O. Guévremont, M. G. Rigamonti, M. Stucchi, F. Cavani, G. S. Patience, Gas-Phase Fructose Conversion to Furfural in a Microfluidized Bed Reactor, *ACS Sustainable Chemistry & Engineering* 6 (4) (2018)
- 565



5580–5587. doi:10.1021/acssuschemeng.8b00510.  
URL <http://pubs.acs.org/doi/10.1021/acssuschemeng.8b00510>

- 570 [50] M. J. Darabi Mahboub, M. Rostamizadeh, J.-L. Dubois, G. S. Patience, Partial oxidation of 2-methyl-1,3-propanediol to methacrylic acid: experimental and neural network modeling, *RSC Advances* 6 (2016) 114123–114134. doi:10.1039/c6ra16605a.  
URL <http://www.scopus.com/inward/record.url?eid=2-s2.0-85006367252&partnerID=MN8TOARS>
- 575 [51] G. G. Nasr, A. J. Yule, L. Bendig, *Industrial sprays and atomization: design, analysis and applications*, Springer Science & Business Media, 2013.
- [52] H. Khan, A. S. Yerramilli, A. D’Oliveira, T. L. Alford, D. C. Boffito, G. S. Patience, Experimental methods in chemical engineering: X-ray diffraction spectroscopy—xrd, *The Canadian Journal of Chemical Engineering* 98 (6) (2020) 1255–1266. doi:<https://doi.org/10.1002/cjce.23747>.
- 580 [53] C. Orr, J. Dallavalle, *Fine Particle Measurement*, Macmillan, N.Y., 1959.
- [54] R. Bardestani, G. S. Patience, S. Kaliaguine, Experimental methods in chemical engineering: specific surface area and pore size distribution measurements—bet, bjh, and dft, *The Canadian Journal of Chemical Engineering* 97 (11) (2019) 2781–2791. doi:<https://doi.org/10.1002/cjce.23632>.
- 585 [55] D. Geldart, Types of gas fluidization, *Powder Technology* 7 (5) (1973) 285–292. doi:10.1016/0032-5910(73)80037-3.
- [56] A. Tube, S. Chamber, F. C. Assembly, Standard Test Method for Determination of Attrition of FCC Catalysts by Air Jets 1, Tech. rep., ASTM (2013). doi:10.1520/D5757-11.2.
- 590 [57] G. S. Patience, R. E. Bockrath, Butane oxidation process development in a circulating fluidized bed, *Applied Catalysis A: General* 376 (2010) 4–12.
- [58] N. Saadatkhah, M. G. Rigamonti, D. C. Boffito, H. Li, G. S. Patience, Spray dried sio<sub>2</sub>, wo<sub>3</sub>/tio<sub>2</sub>, and sio<sub>2</sub> vanadium pyrophosphate core-shell catalysts, *Powder Technology* 316 (Supplement C) (2017) 434–440. doi:<https://doi.org/10.1016/j.powtec.2016.10.056>.
- 595 [59] H. Khan, M. G. Rigamonti, G. S. Patience, D. C. Boffito, Spray dried TiO<sub>2</sub>/WO<sub>3</sub> heterostructure for photocatalytic applications with residual activity in the dark, *Applied Catalysis B: Environmental* 226 (2018) 311–323. doi:<https://doi.org/10.1016/j.apcatb.2017.12.049>.
- 600 [60] K. S. W. Sing, D. H. Everett, R. A. W. Haul, L. Moscou, R. A. Pierotti, J. Roquerol, T. Siemieniewska, *Pure Applied Chemistry* 57 (1985) 603.
- [61] G. S. Patience, *Experimental Methods and Instrumentation for Chemical Engineers*, 2nd Edition, Elsevier B.V., Amsterdam, Netherlands, 2017.